Optical critical dimension measurement of silicon grating targets using back focal plane scatterfield microscopy

Heather J. Patrick
Ravikiran Attota
National Institute of Standards and Technology
100 Bureau Drive
Gaithersburg, Maryland 20899
and
KT Consulting, Inc.
Antioch, California 94509
E-mail: heather.patrick@nist.gov

Bryan M. Barnes
Thomas A. Germer
Ronald G. Dixson
Michael T. Stocker
Richard M. Silver
National Institute of Standards and Technology
100 Bureau Drive
Gaithersburg, Maryland 20899

Michael R. Bishop
International SEMATECH
Montopolis Drive
Austin, Texas 78741

Abstract. We demonstrate optical critical dimension measurement of lines in silicon grating targets using back focal plane scatterfield microscopy. In this technique, angle-resolved diffraction signatures are obtained from grating targets by imaging the back focal plane of a bright-field microscope that has been modified to allow selection of the angular distribution and polarization of the incident illumination. The target line profiles, including critical dimension linewidth and sidewall angle, are extracted using a scatterometry method that compares the diffraction signatures to a library of theoretical signatures. Because we use the zero-order component of the diffraction, the target features need not be resolved in order to obtain the line profile. We extracted line profiles from two series of targets with fixed pitch but varying linewidth: a subresolution 300-nm-pitch series, and a resolved 600-nm-pitch series. Linewidths of 131 nm to 139 nm were obtained, with nanometer-level sensitivity to linewidth, and a linear relationship of linewidth obtained from scatterfield microscopy to linewidth measured by scanning electron microscopy was demonstrated. Conventional images can be easily collected on the same microscope, providing a powerful tool for combining imaging metrology with scatterometry for optical critical dimension measurement. © *2008 Society of Photo-Optical Instrumentation Engineers.* [DOI: 10.1117/1.2885275]

Subject terms: optical critical dimension; scatterometry; microscopy; semiconductors; back focal plane; conscopic imaging.

Paper 07011R received Feb. 5, 2007; revised manuscript received Sep. 28, 2007; accepted for publication Nov. 27, 2007; published online Mar. 13, 2008.

1 Introduction

As critical dimension (CD) measurements progress through the 45-nm node and beyond, there is increased urgency to develop techniques that can extend optical microscopy beyond the diffraction limit. While gains can be made by reducing the illumination wavelength and using immersion optics, another class of interrelated optical techniques, which include scatterometry, critical dimension spectroscopic ellipsometry, and optical critical dimension metrology, routinely makes measurements on structures smaller than the diffraction limit.[1–3] These techniques extract the line profile, usually including critical dimension linewidth, line height, and line shape, of the lines in a grating target by measuring ellipsometric or reflectance signatures for the target and then comparing the signatures to a library of theoretical signatures to find the best match between theoretical and experimental line profiles. In scatterfield microscopy, we seek to extend signature-based techniques to optical microscopy, extracting critical dimension metrology from unresolved features of targets through comparisons of microscope images with theoretical predictions, using optimized illumination configurations and target designs.[4,5] For example, in a through-focus measurement, the conventional microscope images obtained as a target is moved through the microscope objective focus would be compared to theoretical predictions of the images for different target line profile parameters.[6] Comparing conventional microscope images with theory requires that the spatial and angular properties of the illumination, as well as the collection of the many diffracted orders that recombine to make up the image at the image plane, be extremely well characterized, and that any deviations from ideal be accounted for in the theoretical models.

The current work takes the intermediate steps of looking at the diffracted light from the target directly, by imaging the objective back focal plane, and of separating out the zero-order diffraction to use as the signature. While this aspect of scatterfield microscopy is based upon a well-known imaging method,[7] and semiconductor metrology systems based on this general technique have been described in previous patents[8–10] and proceedings,[11,12] the work presented here reviews in detail the advantages of using an illumination mask to control incident angles and allow separation of the specular and higher diffraction orders, the method used to correct for the effects of angle- and polarization-dependent transmission through the optics by using a bare silicon reference image, and the systematic errors that can arise when using diffraction signatures from back focal plane images. Additionally, while previous authors have also matched back focal plane signatures to theoretical models to extract linewidth and other target parameters,[11,12] we demonstrate here the sensitivity of the method to nanometer-scale changes in the target linewidth.

1537-1646/2008/$25.00 © 2008 SPIE

The robust, repeatable measurement of critical dimension and line profile in grating targets using back focal plane imaging in a bright-field microscope represents a crucial milestone toward full implementation of scatterfield microscopy.

It is well known that diffraction from the sample being imaged appears at the back focal plane of the objective in a bright-field reflection microscope.[7] Light that is diffracted by the sample is collected by the objective if it falls within the cone of angles defined by the objective's collection numerical aperture (NA) and at the objective back focal plane there is a one-to-one mapping of diffraction angle to position. The light illuminating the sample, on the other hand, generally has a range of angles defined by an aperture stop that is located at an aperture plane conjugate to the objective back focal plane. By relaying the diffraction image that appears at the objective back focal plane to a camera (also referred to as conoscopic or Fourier plane imaging), one can collect a diffraction signature for a sample that can then be analyzed using scatterometric techniques.[1–3] As with conventional scatterometry, the target features need not be resolved in order for information to be obtained about them. Variations in linewidth, for example, on a grating target with pitch smaller than the diffraction limit will provide measurable changes in diffraction signature that can be measured at the back focal plane, even though lines on such a target will be unresolved by conventional imaging using the same microscope.

When the illumination is provided from a source with a narrow wavelength range, the diffraction signature is similar to that obtained from conventional, angle-resolved scatterometry.[1] However, while conventional angle-resolved scatterometry typically measures the zero-order, specular reflection component of diffraction in a single plane of incidence perpendicular to the grating lines (varying the incident or polar angle θ at a fixed, $\phi=0$ azimuth angle), the back focal plane image includes all the diffraction from the target over a range of θ' set by the collection NA and a full 360 deg of azimuthal angles ϕ. Depending on the illumination NA and the periodicity of the sample, the diffraction observed at a point on the back focal plane may include contributions from both specular reflectance and higher diffraction orders, potentially complicating the analysis.[8,9] Alternatively, a suitable aperture mask can be placed at the aperture plane to select specific illumination angles. By restricting the illumination angles, the specular reflectance can be separated from higher-order diffraction in the back focal plane image and be independently analyzed, as in conventional scatterometry. This is the approach taken in the present work, and also in Refs. 11 and 12. In Refs. 11 and 12, Petit et al. and Boher et al. used their optical Fourier transform instrument, a dedicated Fourier plane imaging system, to illuminate grating targets using a range of incident angles θ and azimuthal angles ϕ set by an illumination aperture mask. They demonstrated that, as with conventional scatterometry, CD and line profile information could be obtained by comparing the measured specular reflectance with theoretical simulations. They also demonstrated advantages inherent to measuring the diffraction at nonzero azimuths, observing higher-order diffraction from linewidth and line edge roughness that was intentionally engineered into targets, by using nonzero azimuth illumination and detection that would not have been accessible to a conventional $\phi=0$ scatterometer. The use of an illumination aperture mask that is specifically designed to isolate the specular reflectance from higher-order diffraction separates this work and that of Refs. 11 and 12 from other recently described back focal plane imaging systems.[8–10]

In the current work, we demonstrate optical critical dimension measurements of silicon grating targets using back focal plane imaging in a bright-field microscope. The use of a microscope-based system enables us to employ the flexibility of measuring diffraction over a range of incident and azimuthal angles demonstrated by Petit et al. and Boher et al. and also collect conventional images of the targets on the same platform. We use a slit mask at a conjugate back focal plane in the microscope illumination path to restrict the illumination angles at the sample. This allows us to separate the specular reflectance from higher-order diffraction in targets that exhibit multiple diffraction orders. Where Petit et al. and Boher et al. demonstrate one strategy of fixed θ, varying ϕ illumination for separating the diffraction orders for targets with multiple-order diffraction, we here take the approach of varying θ, with ϕ fixed at 0 deg for targets with only zero-order specular reflection, and at a small, nonzero value (typically $\phi=11$ deg) for targets with multiple diffraction orders. Like the variable ϕ technique, this method also serves to isolate the specular reflectance from higher orders, while providing a more conventional reflectance versus incident angle signature.

Using these techniques, we then demonstrate angle-resolved measurements of the zero-order diffraction from two series of targets on a wafer processed using a focus-exposure-matrix (FEM) method: a set of subresolution, 300-nm-pitch targets with only zero-order diffraction, and a set of resolved, 600-nm-pitch targets with multiple diffraction orders. The linewidth and sidewall angle for targets on adjacent dies of the FEM wafer were extracted from the reflectance signatures by comparison with libraries generated by rigorous coupled wave (RCW) analysis using a trapezoidal line profile. Linewidths of 131 nm to 139 nm were obtained, with nanometer-level sensitivity to linewidth, and a linear relationship of linewidth obtained by scatterfield microscopy to linewidth measured by scanning electron microscopy (SEM) was demonstrated. Typical sidewall angles were 86 deg to 87 deg, with no measurable correlation between sidewall angle and SEM linewidth. We also compared extracted linewidths and sidewall angles of the 600-nm-pitch targets with those obtained from atomic force microscopy (AFM). While the AFM measurements indicated that some deviation of the line shapes from the trapezoidal model exists, the scatterfield microscopy linewidths and sidewall angles were in general agreement with those obtained from AFM. Typical short-term uncertainty in scatterfield microscopy linewidth measurement was estimated to be ± 0.8 nm from the repeatability of the measurements. The effects of potential systematic errors, such as bias in the angle calibration at the back focal plane, and deviations of the target heights from the modeled value, are also discussed.

2 Principle of Operation

Figure 1 shows the configuration of the microscope used in this work. Light from an Hg lamp (not shown) is coupled

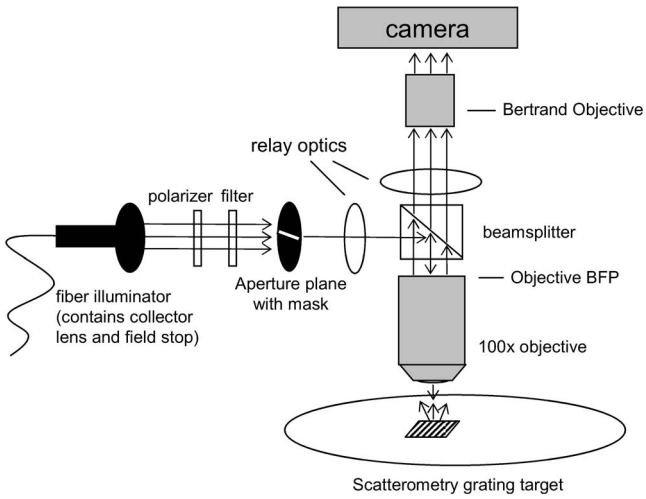

Fig. 1 Schematic of the microscope. The camera collects images of the diffraction from the target, as seen at the objective back focal plane (BFP), by using a Bertrand objective. An additional beamsplitter and relay that are not shown could be used to simultaneously collect conventional images of the target.

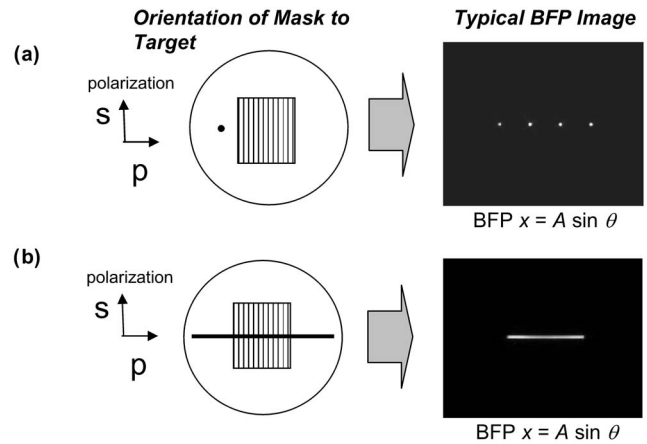

Fig. 2 Examples of illumination masks and the corresponding image that would be acquired by the camera. (a) A small circular aperture selects a nonzero angle of incidence on a grating target with multiple diffraction orders. The $m=-2$, -1, 0, and 1 orders are seen in the BFP image at right. This approach is shown for illustration of the technique only and was not used in the current work. (b) A long slit, perpendicular to the grating ruling, is shown. This slit selects a range of illumination angles, and the image at the BFP corresponds to the diffracted intensity at each collection angle. This approach was employed for the 300-nm-pitch targets.

into a 1-mm-diam. fiber. Light from the fiber end passes through a collector lens and field stop, then through a linear polarizer and filter with a center wavelength of 546 nm. The collector lens images the fiber end to the aperture plane. An amplitude mask is placed at the aperture plane, and its image is relayed to the back focal plane of a 100 $\times$, 0.95 numerical aperture (NA) microscope objective. Because the position at the back focal plane maps to illumination angles at the sample,[7] the illumination amplitude mask serves to select the illumination angles incident upon the sample. The field stop is used to restrict the area of illumination to the desired area of the sample. The light that is diffracted by the sample at angles within the NA of the objective is collected, and an image of the diffraction appears at the back focal plane of the objective. The image of the back focal plane of the objective was relayed to a charge-coupled device (CCD) camera using a Bertrand objective. An additional beamsplitter, which is not shown in Fig. 1, allowed conventional images of the sample to be collected at the same time.

Figure 2 shows an overhead view of the orientation of two illumination masks with respect to the sample. For ease of viewing, the transmissive part of the mask is shown in black. In Fig. 2(a), a simple aperture is shown. If the aperture is small relative to the full back focal plane (shown as the large outer circle), this will select a specific incident angle. In the case of Fig. 2(a), a single, nonzero angle of incidence, θ, is shown for a grating target of 1-μm pitch. The plane of incidence is perpendicular to the grating rulings, at an azimuthal angle $\phi=0$. Because multiple diffraction orders exist for this angle and wavelength, the diffraction pattern image that appears at the back focal plane includes the $m=-2$, -1, 0, and 1 diffraction orders. The position of each order is related to its diffraction angle θ by:

$$x = A \sin \theta, \tag{1}$$

where A is a constant that depends on the magnification of the objective and relay optics to the camera. For our system, the range of collected diffraction angle θ was -71.8 deg to $+71.8$ deg, limited by the NA of the objective. The camera CCD area was 12.3 mm$\times$12.3 mm with 1024×1024 pixels, and the back focal plane image filled a central portion of the CCD. The resolution (in deg/pixel) varies with angle according to Eq. (1); it ranged from roughly 0.5 deg/pixel near $\theta=0$ deg to 0.1 deg/pixel near $\theta=60$ deg.

For the mask shown in Fig. 2(a), collecting diffracted intensity versus θ requires scanning the aperture and collecting an image for each θ. Scanning was not required in the present work. Rather, a mask with a narrow slit as shown in Fig. 2(b) was used. In the case of a zero-order target, that is, a grating with only $m=0$ order diffraction for the objective NA and wavelength used, the slit was not strictly necessary, as for a zero-order target each position in the back focal plane contains only zero-order diffraction from a unique incident angle. For these targets, the slit was oriented perpendicular to the grating lines at $\phi=0$ and was used to clearly define the range of diffraction angles to be analyzed in the back focal plane image. For targets with multiple diffracted orders, orienting the slit perpendicular to the target lines results in overlapping diffracted orders in the back focal plane image. In this case, the slit was angled slightly off the normal to the lines, at an azimuthal angle of $\phi=11$ deg, such that the higher orders were separated from the $m=0$ order, as shown in Fig. 3. While this was necessary in order to isolate the desired zero-order diffraction intensity from higher orders, it did result in more complex theoretical calculations due to the requirement that conical diffraction geometry be considered.

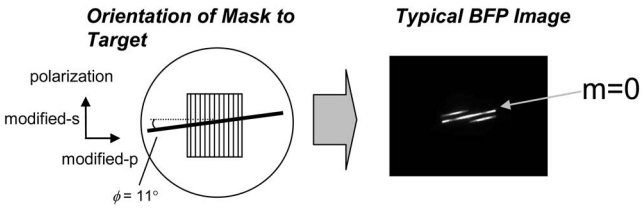

Fig. 3 Rotated orientation of the slit with respect to the target, used for the 600-nm-pitch targets where the target pitch caused multiple diffraction orders to be present. The rotation causes the $m=0$ order to be separated from higher orders at the BFP. The slit angle was roughly $\phi=11$ deg. Polarizations were defined with respect to the lines; because they are not purely s- or p-polarization with respect to the plane of incidence, they are referred to as modified-s and modified-p.

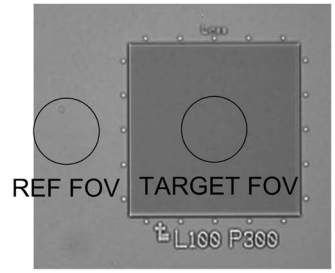

Fig. 4 Low-magnification image of a typical grating target (target lines are unresolved), and illustration of the field of view (FOV) used for data collection. When collecting data, the field stop was reduced to restrict the area of illumination to a central area of the target (TARGET FOV) or to an area of bare silicon for the reference image (REF FOV), as shown. This image was obtained using a 10× objective, while a 100× objective was used for actual data collection.

In addition to the angular selection made by the illumination mask, the polarization of the incident light was also controlled. For all targets, images were collected both with the electric field vector perpendicular to the plane of incidence (s-polarization) and with the electric field vector in the plane of incidence (p-polarization). An exception to this was made when the slit was angled for examining higher-order targets; the polarization was selected to be along the grating lines (modified-s) or perpendicular to the grating lines (modified-p), although the plane of incidence was rotated slightly from the grating lines.

3 Data Collection and Conversion to Reflectance Signature

Back focal plane images were obtained from 100 μm $\times$100 μm scatterometry targets. The targets were produced using the SEMATECH Overlay Metrology Advisory Group 3 (OMAG3) reticle.[13] The targets were etched silicon line gratings on a silicon substrate. The wafer was produced using a focus exposure matrix, such that targets on adjacent dies had fixed pitch, but different linewidths. The linewidths at the bottom of the line profile as measured by SEM varied from 150 nm to 158 nm. Two series of targets were investigated: zero-order targets of 300-nm pitch, and 600-nm pitch targets for which multiple diffraction orders were present.

For a typical data run, back focal plane images were taken for a series of targets of fixed pitch at nine adjacent dies on the wafer. At each location, two images were taken for the two linear polarizations. The approximate locations of the images are shown in Fig. 4. The first image was a target image. The target was brought into focus below the objective, with the microscope field stop reduced so that the illumination spot was restricted to a central region of the target, approximately 30 μm in diameter. The second image was taken on a flat area of silicon adjacent to the target and was considered to be a reference image. In addition, a dark current image was taken for each data series, with no light reaching the camera.

A raw back focal plane image from a 300-nm-pitch target appeared as a horizontal line, as shown in Fig. 2(b). After subtracting the dark current image, the target and reference images were converted to intensity in digital numbers (DN) from the camera CCD versus angle. The conversion factor A from back focal plane x direction to θ in Eq. (1) was calibrated by fitting back focal plane images of the diffraction peaks from 2.75-μm and 1.98-μm pitch targets illuminated at 0 deg using a pinhole aperture mask. The illumination angular range of the data images was approximately −60 deg to +60 deg and was limited by the size of the image of the illuminating fiber end at the conjugate back focal plane rather than by the NA of the objective. The polarization extinction of the light from the objective was verified to be better than 30:1. The bright line of the back focal plane image shown in Fig. 2(b) was roughly 10 pixels high; data were averaged across the central six pixels of the image to obtain a single intensity value for each angle θ.

The intensity versus angle data measured from the s-polarization and p-polarization images of a 300-nm-pitch target are shown in Fig. 5(a). Due to angle- and polarization-dependent variations in transmission through the illumination and collection optics, as well as uncorrected variations in the source intensity versus angle, these curves do not represent the true reflectance versus angle signatures of the target. In order to obtain reflectance signatures that could be compared with theory, the target intensity versus angle data were corrected using intensity data from bare silicon reference images like the one shown in Fig. 5(b). The apparent noise in the data shown in Figs. 5(a) and 5(b) was highly repeatable and represents the inhomogeneity in the source intensity versus angle. Since bare silicon exhibits a well-known reflectance versus angle and polarization that can be calculated from its optical constants, we used the intensity data from the bare silicon reference image to calculate a correction for the effects of source inhomogeneity and polarization-dependent transmission, to be applied to the target intensity data. The calculated reflectance versus angle for s- and p-polarization of silicon, including a 1.6-nm layer of native oxide assumed to be on the surface due to exposure to air, is shown in Fig. 5(c). The differences between the curves shown in Fig. 5(b) and Fig. 5(c) represent the cumulative effects of angle- and polarization-dependent transmission through the illumination and collection optics and the nonuniformity of the light source intensity versus angle.

To convert the raw target data shown in Fig. 5(a) to the target reflectance versus angle shown in Fig. 5(d), we divide the data in Fig. 5(a) by that in Fig. 5(b) and multiply the result by that in Fig. 5(c). The resulting target reflec-

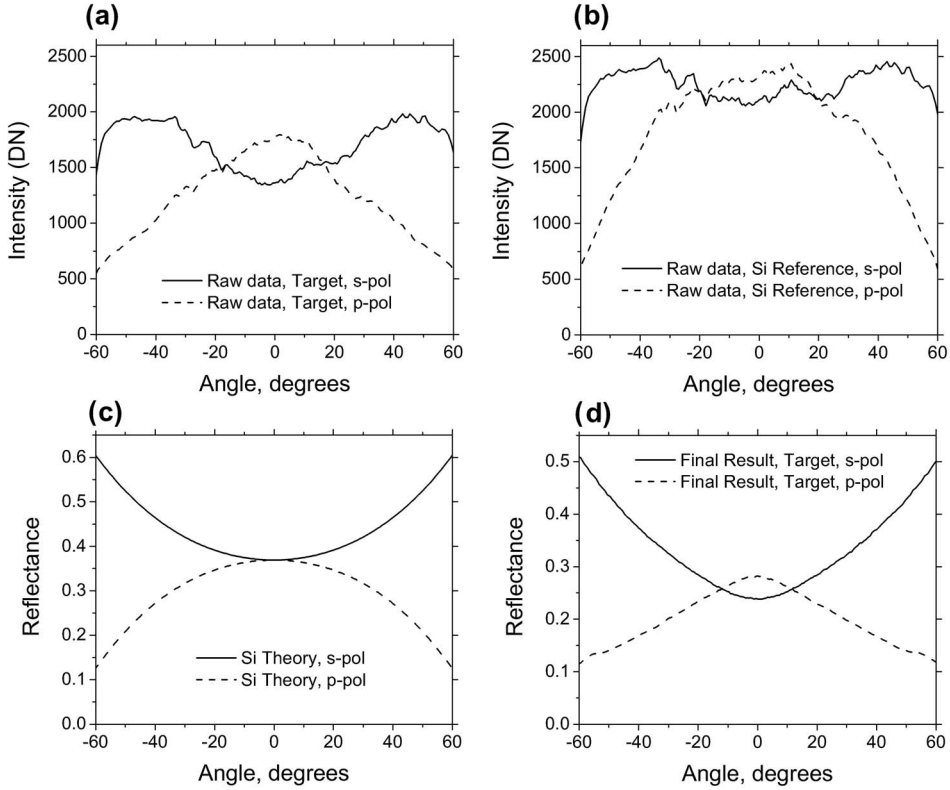

Fig. 5 Data analysis using silicon reference image and calculated silicon reflectance curve, as discussed in the text. Graph (a) shows the raw data for (solid line) s-polarization and for (dashed line) p-polarization, taken from the target BFP image and reduced to intensity versus angle. The raw data is corrected using a reference BFP image (b) taken from a flat silicon area next to the target and the calculated reflectance (c) of silicon versus angle. The final results for reflectance versus angle (d) for the target are obtained for each polarization by dividing the data in (a) by that in (b) and then multiplying by the data in (c).

tance, shown in Fig. 5(d), was smoothly varying with very little apparent noise. The same type of correction was made on the specular, $m=0$ component of the data taken for the 600-nm-pitch targets using the rotated slit (Fig. 3), except that the silicon reflectance was calculated using the modified-s and modified-p polarizations. The transmission correction via bare silicon reference image works well for the specular reflection component of the target diffraction, where, as for the bare silicon, the incident and diffracted angles are equal. If we wanted to convert the intensity of higher-order diffraction to absolute diffraction efficiency relative to the incident light, however, the bare silicon reference would be insufficient: due to the different diffraction angle, the transmission correction for the higher-orders is not obtained from the silicon reference image. The restricting of the illumination angles via a mask, and the resulting separation of the specular order from higher-order diffraction, is essential to allowing the back focal plane images to be converted to reflectance and analyzed using standard specular scatterometry techniques.

4 Modeling of Reflectance Signatures

We extract line profile information from the reflectance signatures of the targets by comparing them to a library of simulated signatures generated using RCW analysis. The simulated signatures were produced using the method for surface relief gratings developed by Moharam et al.,[14,15] with a modification suggested by Lalanne and Morris[16] to improve the convergence of the theory for p-polarization. The solution requires Fourier series expansion of the periodic dielectric function for each layer, and in practice, this series is truncated at some maximum order N. In the current work, we truncated the series at $N=50$ to ensure adequate convergence of the results.

The modeled profile for a single line in the grating target is shown in Fig. 6. The line profile of the targets was taken to be a single trapezoid characterized by its height, bottom linewidth, and sidewall angle. To approximate this in the model, each line was divided into seven layers, two of which were used to account for the presence of a thin layer of native oxide on the silicon due to atmospheric exposure, and the other five used in a staircase approximation to simulate the sidewall angle.[17] As a check, a limited number of simulations were also run with ten layers in the sidewall, but this did not give appreciably improved results over the less computationally intensive five-layer case. The native oxide layer was taken to be 1.6-nm-thick, with $n=1.7363$ and $k=0$ (Ref. 18). The modeled bottom linewidth includes twice the thickness of this oxide layer. The substrate and grating lines were silicon and were assumed to have optical properties of $n=4.0883$ and $k=0.02577$ (Ref. 18). The same optical constants were used when calculating the reference reflectance of bare silicon shown in Fig. 5(c).

As is typical in scatterometry, reference metrology from

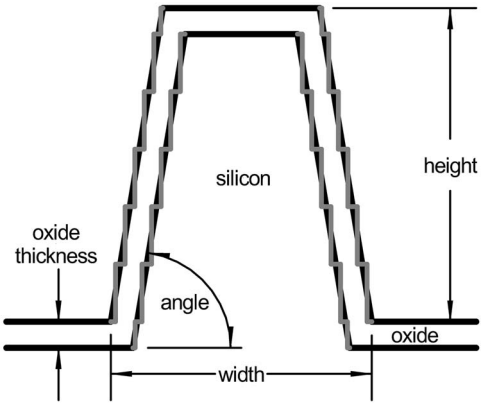

Fig. 6 Line profile used in model. The line profile was approximated as a trapezoid using a staircase approximation to simulate the sidewall angle. The thickness of the native oxide layer has been greatly exaggerated.

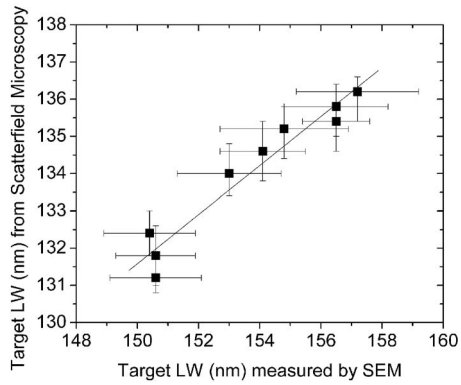

Fig. 8 Bottom linewidth (LW) obtained from library matching of the scatterfield microscopy curves versus bottom linewidth as measured by SEM, for nine 300-nm-pitch targets from different dies of the FEM wafer (solid squares) and linear fit to the data (solid line).

other methods was used as inputs to the model, in determining both the line profile used in generating the library and the range of library parameters. Our reference metrology included SEM measurements of the pitch and bottom linewidths of all the targets and AFM measurements of height and line profile on the 600-nm-pitch targets. The pitch was well known and was not expected to vary from target to target. For the nominally 300-nm-pitch targets, we set pitch=302 nm, and for the nominally 600-nm-pitch targets, we set pitch=602 nm, which were the values given by the SEM measurements. The height was not expected to vary from target to target, and the AFM measurements on the 600-nm-pitch targets confirmed this. Using an initial set of three targets, we measured a preliminary value for the height of 228.4 nm; when generating the libraries used in the primary data analysis shown in Figs. 7–10, the height was fixed at this value for both the 300-nm and 600-nm-pitch targets. Later AFM data taken over all of the 600-nm-pitch targets in this investigation confirmed this average height; additionally, the effect of varying the height is presented in the discussion.

For the data analysis of Figs. 7–10, libraries were generated varying the two remaining parameters, linewidth and sidewall angle. The SEM and AFM measurements for linewidth and sidewall angle were used to determine the ranges of these parameters to be included in the libraries, and the linewidth was varied in 0.2-nm increments, with the sidewall angle varied in 0.2-deg increments. The reflectance curves for s- and p-polarization for a given target were then compared to the appropriate pitch library, and the best-fit curves determined by minimizing the mean-squared difference of the data to the theoretical curves.[1] The s- and p-curves were compared simultaneously so that a single set of best-fit linewidth and sidewall angle were determined for each target. Interpolation between model intervals was not used when determining the best-fit linewidth and sidewall angle. In the case of the 600-nm-pitch targets, due to the angling of the illumination slit, the incident angles had a nonzero azimuthal component, and the polarization was along the target lines and not exactly perpendicular to the plane of incidence. This was taken into account in the models when generating modified-s and modified-p theoretical curves for these targets.

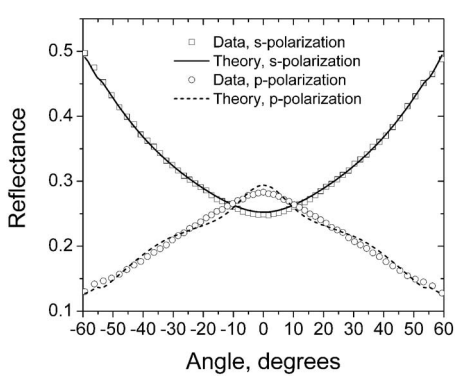

Fig. 7 Reflectance data and theoretical reflectance for a typical 300-nm-pitch target. Results for s-polarization are shown as open squares (data) and solid line (theory). Results for p-polarization are shown as open circles (data) and dashed line (theory).

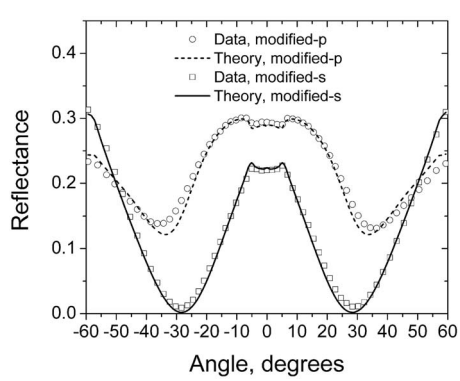

Fig. 9 Reflectance data and theoretical reflectance for a typical 600-nm-pitch target. Results for modified-p polarization are shown as open circles (data) and dashed line (theory). Results for modified-s polarization are shown as open squares (data) and solid line (theory).

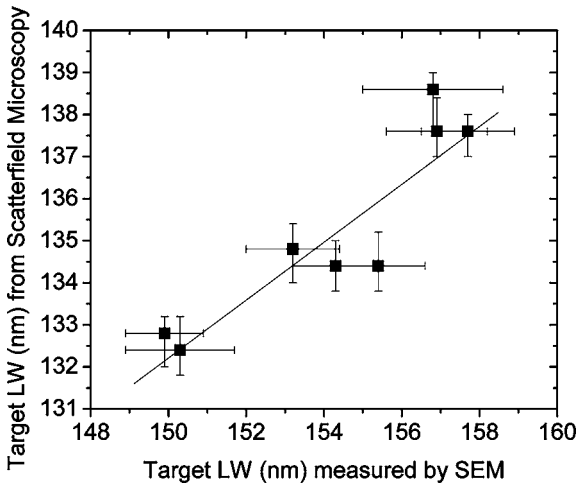

Fig. 10 Bottom linewidth (LW) obtained from library matching of the scatterfield microscopy curves versus bottom linewidth as measured by SEM, for eight 600-nm-pitch targets from different dies of the FEM wafer (solid squares) and linear fit to the data (solid line).

5 Results

For the 300-nm-pitch targets, reflectance curves for nine targets at different positions on the FEM wafer were obtained. The data and best-fit theory for a typical target are shown in Fig. 7. The shapes of the s- and p-data curves were highly repeatable over multiple data collection runs of a given target taken on multiple days, and typical day-to-day repeatability of the reflectance at a fixed angle for a given target (taken over nine total runs in three days) was 1%. The theoretical curves shown in Fig. 7, which represent the best-fit linewidth and sidewall angle from the library, have a sidewall angle of 86.8 deg and a linewidth of 134.6 nm. Fig. 8 shows the bottom linewidth obtained from the best fit to the scatterfield microscopy reflectance signatures versus the bottom linewidth measured by SEM for all nine targets. A linear correlation between linewidth extracted from scatterfield microscopy and linewidth measured by SEM was obtained, with nanometer-level sensitivity of the scatterfield microscopy results to changes in linewidth. The nonzero offset between the optical measurements and the SEM measurements, discussed further later in this paper, is not unusual when comparing optical and SEM techniques.[19,20] The sidewall angles obtained from the best fits to the reflectance signatures were between 86.4 deg and 87.0 deg for all nine targets and were not correlated with position on the FEM wafer or the target linewidth that was measured by SEM.

Figure 9 and 10 show reflectance curves for a typical target and the results for scatterfield microscopy linewidth versus SEM linewidth for the eight of the nine targets of 600-nm pitch. The reason for excluding one of the targets is discussed later. For the 600-nm-pitch targets, the illumination slit was angled relative to the target lines as shown in Fig. 3, and only the $m=0$ data was analyzed, so that the data in Fig. 9 represent the specular reflectance signature of this target. Polarizations are referred to as modified-s and modified-p to indicate that due to the slit angle, the incident polarizations were not fully within or perpendicular to the plane of incidence, an effect that was accounted for in the model. The linewidth and sidewall angle for the best-fit theory shown in Fig. 9 were 134.4 nm and 86.2 deg, respectively. As with the 300-nm-pitch targets, the 600-nm-pitch targets showed a linear correlation between linewidth extracted from scatterfield microscopy to linewidth measured by SEM, as shown in Fig. 10, and sensitivity to changes in linewidth on the nanometer scale. While the straight line fit of linewidth from scatterfield microscopy to linewidth measured by SEM was not quite as good here as with the 300-nm-pitch targets shown in Fig. 8, especially in the 153-nm to 156-nm range, given the extent of the error bars shown in Fig. 10 and discussed in more detail later, we believe the linear fit to be reasonable. The sidewall angle from scatterfield microscopy varied from 85.8 deg to 86.4 deg, with no correlation of sidewall angle to linewidth measured by SEM or position on the FEM wafer. Similar to the 300-nm pitch targets, there was a nonzero offset between the optical linewidths and the SEM measured linewidths.

In Figs. 8 and 10, we include uncertainty estimates on both the SEM linewidth measurements and the linewidths extracted from the library fitting of the scatterfield microscopy reflectance signatures. The horizontal error bars shown in Figs. 8 and 10 represent a single standard deviation of 27 SEM measurements of bottom linewidth made on each target. The vertical error bars are derived from the short-term repeatability of the reflectance signatures of the targets. The short-term repeatability, rather than the day-to-day repeatability mentioned earlier, was used because all data points within Fig. 8 or Fig. 10 were taken within a single, few-hour data run. The short-term repeatability was estimated as follows. On two occasions, we obtained ten consecutive silicon reference images, analyzed these to obtain intensity versus angle, and derived the standard deviation of the intensity at each fixed angle. For the worst case of these two tests, the typical standard deviation of intensity at fixed angle was 0.7%, independent of angle, primarily manifested as a shift of the overall intensity curve versus angle. As each target measurement is normalized to a reference measurement when calculating reflectance, and because we expect similar repeatability in target and reference intensity, the percentage uncertainty for reflectance of a target was estimated by multiplying the preceding standard deviation by a factor of $2^{1/2}$. Once the standard deviations for the target reflectance signatures were thus determined, we calculated the vertical error bars shown in Figs. 8 and 10 by shifting the actual reflectance signatures for each target up and down by one standard deviation and comparing these shifted signatures to the library. Because the change in best-fit linewidth is not in general linear with changes in the reflectance, the vertical error bars in Figs. 8 and 10 vary somewhat from target to target and also can give unequal positive and negative error for the same target. The linear fits in Figs. 8 and 10 were produced from weighted linear regression, using as the vertical uncertainty the larger of the positive and negative error bars from each target. For Fig. 8, the linear fit has a slope of 0.66 ± 0.09 and an intercept of 32.8 nm $\pm$ 14.3 nm. For Fig. 10, the fit has a slope of 0.69 ± 0.10 and an intercept of 29.0 nm $\pm$ 14.9 nm. Thus within the uncertainty, we obtain the same fit of scatterfield microscopy extracted linewidth

to SEM linewidth for both unresolved, 300-nm-pitch targets and for 600-nm-pitch targets with multiple diffraction orders.

The existence of an offset between scatterfield-microscopy-determined linewidth and SEM-determined linewidth, as well as the nonunity slope between them, are not unique to the present work and have been seen previously when comparing optical-signature-based and SEM-based measurements.[19,20] It may result from limitations of the simple profile chosen for the modeling, for example, choosing a single trapezoid to approximate the profile and not including corner rounding.[21] It may also include contributions from the accuracy of the SEM linewidth measurement, which has good sensitivity to small changes in linewidth but may exhibit an offset in linewidth accuracy that depends on the edge detection algorithm and line shape. To aid in the evaluation of the accuracy of the scatterfield microscopy measurements, we also compared the results from the scatterfield microscope to AFM measurements of the targets in the 600-nm-pitch series. Using AFM measurements of the line profile, we extrapolated bottom linewidth and sidewall angle for the eight targets represented in Fig. 10. The bottom linewidths measured by AFM ranged from 130.0 nm to 139.5 nm, compared with a range for the scatterfield microscopy data of 132.4 nm to 138.6 nm. The sidewall angles extracted from AFM ranged from 87 deg to 87.6 deg, compared with a range of 85.8 deg to 86.4 deg from scatterfield microscopy, and as in the scatterfield microscopy case, there was no correlation of sidewall angle to linewidth measured by SEM or position on the wafer. An individual AFM measurement of bottom linewidth had an expanded uncertainty of ± 4 nm, while the uncertainty in AFM sidewall angle was estimated at ± 1 deg, putting the scatterfield microscopy bottom linewidths and sidewall angles in reasonable agreement with the AFM measurements. As with the comparison with SEM data in Fig. 10, the linewidth from scatterfield microscopy exhibited a linear trend with increasing AFM linewidth, with a subunity slope between scatterfield microscopy and AFM results. However, there was some scatter in this data. The AFM measurements also indicated that the lines are not ideal trapezoids but include some corner rounding and nonlinearity along the sidewall that may complicate the comparison of AFM and scatterfield microscopy results. Nonetheless, we are encouraged that the scatterfield microscopy linewidths generally fell within a few nanometers of those measured by AFM, given the accuracy and traceability of AFM linewidth measurements.[22] The nonunity slope of scatterfield microscopy linewidth to that measured by both SEM and AFM may arise from the simplified line profile assumed by the trapezoidal model. Improved correlation to SEM and AFM measurements may well be obtained by including multiple trapezoids, corner rounding, or other modifications.[21]

As mentioned earlier, there was an additional, ninth target in the 600-nm-pitch series that was measured both by scatterfield microscopy and by AFM, but that was not included in Fig. 10. This was a target with SEM-measured linewidth of 146.1 nm. For this target, using the scatterfield microscope, the best-fit model linewidth was 133.2 nm, and the best-fit sidewall was 85.2 deg. If this target had matched the trend shown by the other eight targets, then using the linear fit shown in Fig. 10, we would have expected a sidewall angle between 85.8 deg and 86.4 deg and a linewidth of 129.8 nm. The AFM measurements also indicated a low sidewall angle for this target (86.7 deg compared to the 87 deg to 87.6 deg range found for the other eight targets), and the difference between the top and midpoint AFM linewidth for this target was 15 nm, compared to a typical 7-nm difference for the other targets. For these reasons, this anomalous target has been excluded from Fig. 10.

6 Discussion

For the analysis shown in Figs. 7 to 10, the line height was held fixed in the simulations. This was done in order to speed up calculations, and also because AFM measurements on the 600-nm targets indicated that the height was constant to within nanometers. In the original libraries, the height was held fixed at 228.4 nm. To check the sensitivity to height variation, we generated additional libraries using fixed heights of either 227.2 nm or 229.7 nm, which were the minimum and maximum heights measured for all of the nine 600-nm-pitch targets (including the anomalous target excluded from Fig. 10) investigated using AFM. We then fit the reflectance data from the 300-nm and the 600-nm target sets to these libraries. The overall effect was to shift all of the linewidths for a same pitch set of targets up or down by an average of ± 0.3 nm, giving a systematic uncertainty in the linewidth accuracy but not changing the linear trend of extracted linewidth to SEM linewidth seen in Fig. 8 and Fig. 10. Although only the 600-nm-pitch targets, and not the 300-nm-pitch, were measured by AFM, we believe it is unlikely that the target height varied greatly between the two sets.

It can be observed in Fig. 7 that there is some deviation of the theory and the data, particularly for the p-polarization results, consisting of an additional, higher-frequency component to the theoretical signature that is not seen in the experimental signature. This higher-frequency component was present to some degree in all of the best-fit p-polarization theoretical curves for the 300-nm-pitch targets, while absent in the experimental data. It is possible that this effect arises from linewidth or line edge variation across the target that is not considered in the model. We have recently shown[23] that the presence of random edge variation, for example, can reduce the amount of structure seen in a target's reflectance signature compared to the signature produced from a target with no edge variation.

Another potential source of deviation between theory and experiment for this type of scatterfield measurement is the quality of the angle calibration. The requirement for a reference image and the calibration of the target image reflectance from the reference, while giving good repeatability and sensitivity, has the potential to introduce errors in reflectance accuracy, particularly at large incident angles for p-polarization. The final value for target reflectance at a given angle depends on the determination of the constant A in Eq. (1), not only as a scaling from x to θ, but also because the values of the theoretical silicon reflectance curve are calculated using θ. The nonlinear relationship between A and θ makes the effect larger at high angles of

incidence. For example, a 1% change in A at a value of x that corresponds to $\theta=10$ deg changes the calculated θ by only 0.1 deg, but at a value of x that corresponds to $\theta=60$ deg changes the calculated θ by 1 deg. This effect is compounded by the nonlinear change in silicon reflectance versus angle, which also has a steeper slope at higher angles (over the range used here). At $\theta=10$ deg, a $\Delta\theta=0.1$ deg changes R_p and R_s of silicon only by ~ 0.0001 (out of $R_s=0.37$ or $R_p=0.36$), while at $\theta=60$ deg, a $\Delta\theta=1$ deg changes R_p and R_s of silicon by ~ 0.009 (out of $R_s=0.61$ or $R_p=0.12$). Since the target data is multiplied by the silicon R_p or R_s, this leads to a worst-case change in the calculated target reflectance corresponding to a given value of back focal plane x of 7.5%, for p-polarization at $\theta=60$ deg. This does not change the sensitivity of the system, as once a value for A has been chosen, all reflectance curves are calculated using the same silicon reflectance values, but rather changes the accuracy of the reflectance measured at a given angle.

This effect may partially account for the type of discrepancy between theory and experiment shown at higher angles in Fig. 9 for modified-p polarization. We estimate the current uncertainty in our determination of A at $\pm 0.5\%$, primarily from the uncertainty of the pitch of the targets used in its calculation. In order to quantify the effect of the angle calibration on the extracted linewidth, we recalculated the reflectance signatures of both the 300-nm and 600-nm target groups using $A \pm 0.5\%$, and compared the resulting signatures to the libraries. For the 600-nm targets, the typical change in linewidth was ± 0.5 nm. As expected, the overall effect was to shift all the linewidths for the 600-nm targets up or down, giving a systematic uncertainty in the linewidth accuracy but not changing the linear trend of extracted linewidth to SEM linewidth seen in Fig. 10. For the 300-nm targets, the effect of shifting $A \pm 0.5\%$ was nearly negligible, with typical shifts of 0.2 nm or less. The difference in sensitivity to A between the two groups of targets arises from the different polarization and angle sensitivities of their reflectance signatures. For the 600-nm targets, we have observed that the part of the reflectance spectrum with the greatest sensitivity to linewidth is the modified-p polarization from about 30 deg to 60 deg (and from −30 deg to −60 deg). Since variations in A affect primarily the p-polarization signature at large angles, the 600-nm targets are particularly sensitive to angle calibration uncertainty. Another potential source of uncertainty is the correspondence of the actual silicon reflectance to the reflectance calculated from theory. We have performed independent reference measurements of the s- and p-polarized reflectance of silicon surfaces using a laser-based goniometric system,[24] and find that these results are in good agreement with our theoretical predictions.

The uncertainty assigned to the scatterfield microscopy linewidth in Figs. 8 and 10 represents the repeatability component of the uncertainty in the measurement and is ± 0.8 nm for a typical target. In addition to this component, we have also identified systematic errors on the order of ± 0.3 nm from possible variations of the target height from the assumed value, and of ± 0.5 nm for the 600-nm-pitch targets from the uncertainty in the angle calibration of Eq. (1). These systematic components of the uncertainty do not affect the demonstrated sensitivity of back focal plane scatterfield microscopy to nanometer-scale changes in linewidth but do place limits on the overall accuracy of the measurements. Sources of remaining differences between linewidths measured by scatterfield microscopy to those measured by SEM and AFM, particularly the nonunity slope, may include the effects of linewidth and line edge variation on the reflectance and deviations from the simple trapezoidal line shape assumed in the RCW analysis. The trapezoidal model used here is simply parameterized, gives reasonable fits to the data within the parameter space expected from reference metrology of the targets, and quantifies the sensitivity of the measurement, but other models may give improved fits to the measured reflectance spectra and more accurate parameterization of the target lines.

In terms of improving the performance of back focal plane scatterfield microscopy, a large component of the uncertainty in repeatability arises from the short-term stability of the Hg lamp light source, as separate target and reference images are needed to create a reflectance signature. This could be improved by stabilization or monitoring of this source. It is also possible to collect reflectance signatures from target and bare Si simultaneously from a series of conventional images taken using a scanning aperture to select a single angle of incidence per image; however, any higher-order diffraction present in the images must then be carefully accounted for in the models.[4] More accurate pitch standards might slightly improve the angle calibration, which was seen to be a significant source of systematic error in the case of the 600-nm targets. Finally, improvements to the illumination and polarization control may be warranted in future systems.

7 Summary and Future Work

In this work, we have demonstrated optical critical dimension measurements using the back focal plane imaging scatterfield microscopy technique. We obtained angle-resolved reflectance signatures, for both subresolution targets exhibiting a single diffraction order and resolved targets with multiple diffraction orders, and compared these signatures with libraries of signatures generated using RCW analysis, to give measurements of the linewidth and sidewall angle of the targets. We show a linear relationship between the linewidth obtained from scatterfield microscopy and the linewidth measured by SEM for a series of targets on a focus-exposure-matrix wafer, and estimate contributions to the linewidth uncertainty from both repeatability and systematic error sources. While the back focal plane scatterfield microscopy technique shares attributes with earlier back focal plane and Fourier imaging work, we have here reviewed in detail the advantages of using an illumination mask to control incident angles and allow separation of the specular and higher-diffraction orders, the method used to correct for the effects of angle- and polarization-dependent transmission through the optics by using a bare silicon reference image and the systematic errors that can arise when using diffraction signatures from back focal plane images. The techniques presented here lay the groundwork for the application of scatterfield microscopy to optical critical dimension metrology, both in back focal plane imaging and in conventional imaging where illumination angle control is employed. Future areas of investigation may include

- Profile analysis of two-dimensional (2-D) targets;
- Improvements in illumination uniformity and polarization control;
- Use of the technique for different target materials and geometries;
- Expanded consideration of uncertainty analysis for this and other signature-based techniques.

Acknowledgment

H. J. Patrick and T. A. Germer acknowledge the use of the NIST Raritan cluster computing system in this work.

References

1. C. J. Raymond, M. R. Murnane, S. Naqvi, and J. R. McNeil, "Metrology of subwavelength photoresist gratings using optical scatterometry," *J. Vac. Sci. Technol. B* **13**(4), 1484–1495 (1995).
2. A. Levy, S. Lakkapragada, W. Mieher, K. Bhatia, U. Whitney, and M. Hankinson, "Spectroscopic CD technology for gate process control," in *Semiconductor Manufacturing Symposium*, 2001 IEEE International, pp. 141–144 (2001).
3. W. Yang, J. Hu, R. Lowe-Webb, R. Korlahalli, D. Shivaprasad, H. Sasano, W. Liu, and D. S. L. Mui, "Line-profile and critical-dimension monitoring using a normal incidence optical CD metrology," *IEEE Trans. Semicond. Manuf.* **17**, 564–572 (2004).
4. R. M. Silver, B. M. Barnes, R. Attota, J. Jun, J. Filliben, M. Stocker, E. Marx, and H. J. Patrick, "Scatterfield microscopy for extending the limits of image-based optical metrology," *Appl. Opt.* **46**, 4248–4257 (2007).
5. T. A. Germer and E. Marx, "Simulations of optical microscope images," in *Metrology, Inspection, and Process Control for Microlithography XX*, C. N Archie, Ed., *Proc. SPIE* **6152**, 61520I1–I11 (2006).
6. R. Attota, R. M. Silver, M. R. Bishop, and R. G. Dixson, "Optical critical dimension measurement and illumination analysis using the through-focus focus metric," in *Metrology, Inspection, and Process Control for Microlithography XX*, C. N Archie, Ed., *Proc. SPIE* **6152**, 61520K1–K11 (2006).
7. S. Inoue and R. Oldenbourg, "Microscopes," in M. Bass, E. W. Van Stryland, D. R. Williams, and W. L. Wolfe, Eds., *Handbook of Optics*, Vol. **II**, 2d ed., pp. 17.39–17.40, McGraw-Hill, New York (1995).
8. J. Opsal and A. Rosencwaig, "Critical dimension analysis with simultaneous multiple angle of incidence measurements," U.S. Patent No. 6,429,943 (6 August 2002).
9. N. Baraket, "Optical system and method for angle-dependent reflection or transmission measurement," U.S. Patent No. 5,889,593 (1999).
10. Y.-H. Chuang, D. Shafer, B.-M. B. Tsai, and J. J. Armstrong, "High-NA system for multiple mode imaging," U.S. Patent No. 7.035,001 (2006).
11. J. Petit, P. Barritault, J. Hazart, P. Chaton, P. Boher, M. Luet, and T. Leroux, "A new analysis strategy for CD metrology using rapid photo goniometry method," in *Metrology, Inspection, and Process Control for Microlithography XIX*, R. M. Silver, Ed., *Proc. SPIE* **5375**, 210–221 (2004).
12. P. Boher, J. Petit, T. Leroux, J. Foucher, Y. Desieres, J. Hazart, and P. Chaton, "Optical Fourier transform scatterometry for LER and LWR metrology," in *Metrology, Inspection, and Process Control for Microlithography XIX*, R. M. Silver, Ed., *Proc. SPIE* **5752**, 192–203 (2005).
13. B. Bunday, M. Bishop, and R. Silver, "The OMAG3 Reticle Set," SEMATECH Document ID# 03074417A, available at www.sematech.org(2003).
14. M. G. Moharam, E. B. Grann, D. A. Pommet, and T. K. Gaylord, "Formulation for stable and efficient implementation of the rigorous coupled-wave analysis of binary gratings," *J. Opt. Soc. Am. A* **12**, 1068–1076 (1995).
15. M. G. Moharam, D. A. Pommet, E. B. Grann, and T. K. Gaylord, "Stable implementation of the rigorous coupled-wave analysis for surface-relief gratings: enhanced transmittance matrix approach," *J. Opt. Soc. Am. A* **12**, 1077–1086 (1995).
16. P. Lalanne and G. M. Morris, "Highly improved convergence of the coupled-wave method for TM polarization," *J. Opt. Soc. Am. A* **13**, 779–784 (1996).
17. S. T. Peng, T. Tamir, and H. L. Bertoni, "Theory of periodic dielectric waveguides," *IEEE Trans. Microwave Theory Tech.* **MTT-23**, 123–133 (1975).
18. C. M. Herzinger, B. Johs, W. A. McGahan, J. A. Woollam, and W. Paulson, "Ellipsometric determination of optical constants for silicon and thermally grown silicon dioxide via a multi-sample, multi-wavelength, multi-angle investigation," *J. Appl. Phys.* **83**, 3323–3336 (1998).
19. W. Yang, J. Hu, R. Lowe-Web, R. Korlahalli, D. Shivaprasad, H. Sasano, W. Liu, and D. S. L. Mui, "Line-profile and critical-dimension monitoring using a normal incidence optical CD metrology," *IEEE Trans. Semicond. Manuf.* **17**, 564–572 (2004).
20. P. Reinig, R. Dost, M. Mört, T. Hingst, U. Mantz, J. Moffitt, S. Shakya, C. J. Raymond, and M. Littau, "Metrology of deep trench etched memory structures using 3-D scatterometry," in *Metrology, Inspection, and Process Control for Microlithography XIX*, R. M. Silver, Ed., *Proc. SPIE* **5752**, 559–569 (2005).
21. C. J. Raymond, S. Sohail, H. Naqvi, and J. R. McNeil, "Resist and etched line profile characterization using scatterometry," *Proc. SPIE* **3050**, 476–486 (1997).
22. R. G. Dixson, R. A. Allen, W. F. Guthrie, and M. W. Cresswell, "Traceable calibration of critical-dimension atomic force microscope linewidth measurements with nanometer uncertainty," *J. Vac. Sci. Technol. B* **23**, 3028–3032 (2005).
23. T. A. Germer, "Effect of line profile variation on specular and diffuse reflectance from a periodic structure," *J. Opt. Soc. Am. A* **24**, 696–701 (2007).
24. T. A. Germer and C. C. Asmail, "A goniometric optical scatter instrument for bidirectional reflectance distribution function measurements with out-of-plane and polarimetric capabilities," in *Scattering and Surface Roughness*, Z.-H. Gu and A. A. Maradudin, Eds., *Proc. SPIE* **3141**, 220–231 (1997).

Heather J. Patrick has worked for KT Consulting, Inc., under contract to the National Institute of Standards and Technology in Gaithersburg, Maryland, since 2005. Her research focuses on optical dimensional metrology of patterned nanoscale materials using signature-based scatterometric and ellipsometric techniques. Dr. Patrick's interests span a broad range of applications of optical technology, and her career has included positions as a principal scientist at optical communications start-up Optinel Systems in Elkridge, Maryland, and as a staff scientist at the Naval Research Laboratory in Washington, DC, where she developed fiber optic sensors for structural health monitoring and guidance systems. Dr. Patrick holds 2 U.S. patents and is the author of numerous journal articles. She received her SB degree in physics from the Massachusetts Institute of Technology, and her PhD degree in physics from the University of Colorado, Boulder.

Ravikiran Attota received his PhD in mechanical engineering from Indian Institute of Science, Bangalore, India with specialization in tribology of ceramics. In 1996 he worked as a Humboldt (AvH) fellow in Germany. Following this he worked for Data Storage Institute in Singapore for two years. He has been at the National Institute of Standards and Technology in Gaithersburg, Maryland since 1999. He is currently a research engineer working in the area of optical nano-metrology.

Bryan M. Barnes received his BA degree in mathematics and physics from Vanderbilt University (Nashville, TN, USA) in 1995, progressing to the University of Wisconsin-Madison for his MS and PhD degrees in physics in 1997 and 2004, respectively. He is currently a contractor to the National Institute of Standards and Technology through KT Consulting, Inc. and has worked with the Nanoscale Metrology Group of the Manufacturing Engineering Laboratory of NIST for over two years. Dr. Barnes was awarded an NRC Postdoctoral Fellowship to work with Dr. Richard Silver in 2005.

Thomas A. Germer is a physicist performing research in optical scatter at the National Institute of Standards and Technology. He received his BA degree from the University of California, Berkeley, and his PhD degree from Cornell University. Dr. Germer is a fellow of SPIE.

Ronald G. Dixson completed his PhD in physics in 1994 and has been at the National Institute of Standards and Technology (NIST) for the last 13 years - initially as an NRC postdoc and subsequently on staff. He works primarily on atomic force microscope (AFM) dimensional metrology and standards development at NIST - including the NIST calibrated atomic force microscope (C-AFM) project. Between 2001 and 2004, he spent three years as the first NIST Guest Scientist at SEMATECH where he developed a CD-AFM based Reference Measurement System (RMS) and utilized this system for the 2004 release of single crystal critical dimension reference materials (SCCDRM) to SEMATECH member companies. His current research interests are calibration methods, traceability, and uncertainty analysis in AFM dimensional metrology. He is a member of APS and SPIE.

Michael T. Stocker: biography not available.

Richard M. Silver: biography not available.

Michael R. Bishop is an associate project engineer for lithography metrology at Sematech and ISMI. He has been with Sematech for 19 years, working in all aspects of lithography, and was the process and tool owner for overlay metrology for six years. Currently Bishop supports overlay, CD-SEM and AFM benchmarking and development as well as 450 mm wafer starting materials development. A member of SPIE and the author or coauthor of 40 technical publications, he received a degree in electronic technology from Texas State Technical College in Waco.